Full orientation control of epitaxial MoS$_2$ on hBN assisted by substrate defects

Fu Zhang,[1,2,*] Yuanxi Wang,[2,3,*,†] Chad Erb,[1,4] Ke Wang,[4] Parivash Moradifar,[1,4]
Vincent H. Crespi,[1,2,3,5,‡] and Nasim Alem[1,2,§]

[1]*Department of Materials Science and Engineering, Pennsylvania State University, University Park, Pennsylvania 16802, USA*
[2]*Center for Two Dimensional and Layered Materials, Pennsylvania State University, University Park, Pennsylvania 16802, USA*
[3]*Dimensional Crystal Consortium, Pennsylvania State University, University Park, Pennsylvania 16802, USA*
[4]*Materials Research Institute, Pennsylvania State University, University Park, Pennsylvania 16802, USA*
[5]*Department of Physics, Department of Chemistry, The Pennsylvania State University, University Park, Pennsylvania 16802, USA*

Inversion asymmetry in two-dimensional materials grants them fascinating properties such as spin-coupled valley degrees of freedom and piezoelectricity, but at the cost of inversion domain boundaries if the epitaxy of the grown two-dimensional (2D) layer, on a polar substrate, cannot adequately distinguish what are often near-degenerate 0° and 180° orientations. We employ first-principles calculations to identify a method to lift this near degeneracy: the energetic distinction between eclipsed and staggered configurations during nucleation at a point defect in the substrate. For monolayer MoS$_2$ grown on hexagonal boron nitride, the predicted defect complex can be more stable than common MoS$_2$ point defects because it is both a donor-acceptor pair and a Frenkel pair shared between adjacent layers of a 2D heterostack. Orientation control is verified in experiments that achieve ~90% consistency in the orientation of as-grown triangular MoS$_2$ flakes on hBN, as confirmed by aberration-corrected scanning/transmission electron microscopy. This *defect-enhanced orientational epitaxy* could provide a general mechanism to break the near-degeneracy of 0/180° orientations of polar 2D materials on polar substrates, overcoming a long-standing impediment to scalable synthesis of single-crystal 2D semiconductors.

I. INTRODUCTION

The breaking of in-plane inversion symmetry in polar two-dimensional (2D) crystals such as monolayer MoS$_2$ introduces intriguing physics such as coupled spin-valley degrees of freedom [1,2] and in-plane piezoelectricity [3,4]. Yet such blessings come with a curse: While the interactions of polar 2D layers with near-commensurate polar substrates are typically strong enough to disfavor arbitrary orientations and energetically favor two discrete orientations 180° apart, they are too weak to break the remaining near degeneracy between these two orientations [5,6]. The inversion domain boundaries that then form at the lateral interfaces of merging crystallites [7,8] can degrade device performance [9] and may induce undesirable multilayer growth [10]. Such inversion domain boundaries also complicate the growth of topological insulators such as Bi$_2$Se$_3$ [11], high-T_c superconductors [12], and 3D binary semiconductors [12] (even on carefully chosen lattice-matched substrates). Growth of high-quality single crystals is often associated with the discovery of new physics [13–16]; such growth outcomes have been impeded in polar 2D materials by the ubiquitous presence of inversion grain boundaries.

Prior efforts to suppress inversion domain formation include guiding lateral growth at step edges [11,12] (at the risk of inducing undesirable multilayer growth), or limiting nucleation density [10] (at the cost of slower growth rate). Interesting prior work grew transition metal dichalcogenides (TMD) directly on hexagonal boron nitride (hBN) by powder vapor transport (PVT), chemical vapor deposition [5,6,17–19], or thermal decomposition [20] to achieve scalability better than that of mechanically transferred heterostructures [21–27], but never achieved full orientational epitaxy (i.e., distinguishing inverted domains). The minimum requirement of distinguishing inversion domains in the grown TMD layer is the breaking of in-plane inversion symmetry in the substrate, limiting potential choices to layered compounds such as hBN and semiconductor surfaces such as the (0001) facets of GaN and sapphire. Here we focus on an hBN substrate due to its lack of surface inhomogeneity and dangling bonds [6]. We employ first-principles calculations to identify common intrinsic defects in the hBN substrate that can amplify the distinction between the 0° and 180° stacking geometries and enable full epitaxial growth: a paradoxical *defect-enhanced orientational epitaxy* in which structural defects (in the substrate) *improve* material quality in the layer grown above. Similar orientational control is then observed experimentally by growing MoS$_2$ on exfoliated hBN substrates using PVT, with excellent (~90%) orientational epitaxy. The geometry of the resulting population of triangular flakes is compatible with a near-seamless monolayer containing very few inversion domain boundaries. Aberration-corrected scanning/transmission electron microscopy (AC-S/TEM) confirms the atomic structure and orientation of the MoS$_2$/hBN system.

---

*These authors contributed equally to this work.
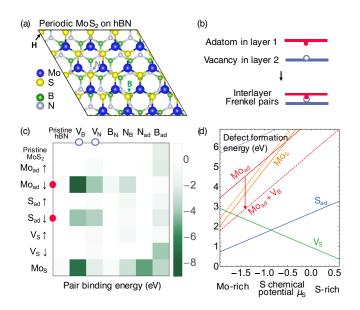†yow5110@psu.edu
‡vhc2@psu.edu
§nua10@psu.edu

FIG. 1. (a) Top view of pristine MoS_2 on hBN, where S atoms sample a variety of local environments, eclipsing B(oron), N(itrogen), or H(ollow) sites. (b) Stable defect pairings in a 2D heterostack are likely Frenkel pairs: an adatom in one layer (red filled) binding strongly to a vacancy in the other layer (blue empty). (c) The $Mo_{ad} + V_B$ complex has the strongest defect pair binding energy (notation described in main text). (d) Formation energies of MoS_2 defects isolated in a monolayer (solid lines), paired with V_B (dashed), and paired with V_N (dotted), as function of sulfur chemical potential and in a nitrogen-rich setting.

II. STACKING DEGENERACY OF INVERSION DOMAINS

We begin by revisiting the difficulty in lifting the $0/180°$ near degeneracy for TMDs stacked on commensurate or near-commensurate substrates. The local minimum energy states for MoS_2 stacked onto itself occurs at $0/180°$ interlayer orientations corresponding to the 2H and 3R polytypes with only a 5 meV difference per MoS_2 unit [28]. The stacking orientation preference of hBN with itself is likewise weak [29]. The orientational preference of a MoS_2 overlayer on a hBN substrate is expected to be even weaker, given their ~28% lattice mismatch. Indeed, density functional theory (DFT) calculations performed with three different implementations of van der Waals (vdW) corrections (DFT-D3 [30], DFT-TS [31], and vdW-DF2 [32]) in a periodic-approximate supercell that contains a 4×4 (5×5) supercell of MoS_2 (hBN) yield a $0/180°$ orientational preference of at most 0.5 meV per MoS_2 unit (see Appendix A for details), where the stacking with reversed bond polarities [defined by elemental electronegativities, see Fig. 1(a)] is only slightly preferred. This near degeneracy is not surprising, since each atom in one layer systematically samples a variety of local environments in the other layer across their interface [Fig. 1(a)]. While this energy difference can be made significant given sufficient area, the energy *barrier* across intermediate orientations between $0°$ and $60°$ ($60°$ is symmetry equivalent to $180°$) also scales with area, and at a faster rate of 2 meV/MoS_2 (see Appendix A), effectively trapping the growing layer at $0°$ or $60°$. The orientation is thus likely set when the MoS_2 flake is

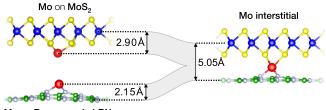too small for the stacking energetics of its interior to overcome thermal fluctuations.

Can the spatial averaging across the supercell be broken by making some specific location(s) in the flake special? Along these lines, we first consider finite-size effects, i.e., edge effects and incomplete spatial averaging, by examining the orientational energetics of finite sulfur-passivated MoS_2 clusters, including those with areas smaller than the smallest possible coincident supercell and the smallest known Mo_xS_y cluster Mo_3S_{13} (see Fig. S1 in the supplemental material [41]). Even in these cases, a marginal preference of at most 2 meV per Mo was found. An intriguing orientation preference found in a recent work differs in that it used Mo_6S_6 clusters with unpassivated metal-terminated edges [33].

III. DISTINGUISHING INVERSION DOMAINS BY A DEFECT COMPLEX

We next consider whether the spatial averaging (and the associated near degeneracy) can be interrupted by a *localized structural defect* in the hBN substrate. Such defects may also act as natural nucleation sites. To find defects that can strengthen interlayer orientational coupling (i.e., correlating the polarities of hBN and MoS_2 more strongly), we systematically examine three types of pairwise interactions: between a MoS_2 point defect and pristine hBN, between an hBN point defect and pristine MoS_2, and between point defects in both MoS_2 and hBN, as tabulated in Fig. 1(c). Darker colors indicate stronger pairwise binding $E_{\text{binding}} = E_{\text{pair}}^{\text{def}} - E_{\text{MoS2}}^{\text{def}} - E_{\text{hBN}}^{\text{def}} - E_{\text{adhesion}}$, where E_{adhesion} is the pristine vdW interlayer adhesion, so that $E_{\text{binding}} = 0$ for pristine MoS_2 stacked on pristine hBN (top left of figure). Mo_{ad}, S_{ad}, V_S, and Mo_S are, respectively, an Mo adatom, S adatom, S vacancy, and Mo substituting S, chosen from common MoS_2 defects with formation energies below 3 eV within the experimentally accessible range of sulfur chemical potentials [34]. The $\uparrow$ and $\downarrow$ symbols indicate MoS_2 defects on the sulfur plane away from or adjacent to the hBN layer. V_B, V_N, B_N, N_B, B_{ad}, and N_{ad}, are B or N vacancies, antisite B or N (i.e., substituting N or B), and B or N adatoms, respectively. We do not consider defects with higher degrees of complexity since they have higher formation energies (see Appendix B) and degrade epitaxy, as discuss later. We find the most strongly bound defects to be proximate adatom-vacancy pairs, with the 9.1 eV $V_B + Mo_{ad}$ binding being by far the strongest. Such combinations are *interlayer Frenkel pairs*: adatom-vacancy complexes that were originally studied for their compliance with charge neutrality and constant stoichiometry (i.e., without electron and elemental reservoirs [35]). Frenkel pairs typically appear as low-energy defect complexes in materials with large differences in cation and anion radii (to accommodate the interstitial), where they leave no detectable remnant if they recombine. In contrast, the "interstitial" in an interlayer Frenkel pair is actually an adatom that is accommodated by the vdW gap, and recombination of the adatom on one sheet with a vacancy in a chemically distinct sheet leaves a distinguishable defect complex, as schematically shown in Fig. 1(b). Since the $V_B + Mo_{ad}$ pair binds the strongest [Fig. 1(c)], we focus on it here and then show that its orientational control function generalizes to other defect pairs such as $V_N + Mo_{ad}$. This

choice is further justified by the calculated formation energies of defect pairs [34,35] $E_{\text{pair}}^{\text{def}} - E_{\text{pristine-MoS2/hBN}} - n_i\mu_i$, where n_i and μ_i are the number of i atoms added or removed from the pristine heterostack and their chemical potentials, with the usual constraint from achieving thermodynamic equilibrium with pristine sheets $\mu_{\text{Mo}} + 2\mu_S = E_{\text{MoS2}}$ and $\mu_B + \mu_N = E_{\text{hBN}}$. Defect pair formation energies are shown in Fig. 1(d) as functions of μ_S (referenced from the per-atom energy of solid α-S) and for μ_N set to the per-atom energy of N$_2$ (the nitrogen-rich limit [36]): Among the various defects in MoS$_2$, Mo$_{\text{ad}}$ (solid red) is the only defect that is stabilized when paired with V$_B$ (dashed red). (If X is an isolated MoS$_2$ defect, the $X + V_B$ binding energy needs to be stronger than V$_B$ formation energy to stabilize $X + V_B$ against X [35]). We therefore exclude other defect combinations involving, e.g., S$_{\text{ad}}$ or Mo$_S$ for the present study. Defect formation energies from hybrid functional calculations are also shown in Fig. S2. Even though the Mo$_{\text{ad}} + V_B$ formation energy of at least 2 eV would still yield a negligible defect concentration, hBN defects should be preexisting so that the V$_B$ contribution to the formation energy need not be accounted for. The native V$_B$ in hBN before MoS$_2$ growth are expected to be out-of-equilibrium and passivated by hydrogen, since hBN samples are synthesized from hydrides and since H-passivated V$_B$ is ~7.7 eV more stable than V$_B$ [36], with a large migration barrier rendering them immobile below their annealing temperature of at least ~$1000-2000$ K [36]. Thus, taking the fully passivated V$_B$ + 3H complex as immobile (out of equilibrium), taking Mo$_{\text{ad}}$ as mobile (in equilibrium) with formation energy E_{Mo}, and taking their binding energy as $E_{\text{binding}} = E_{\text{VB+3H}} + E_{\text{Mo}} - 3\mu_H - E_{\text{VB+Mo}}$ (positive for Mo replacing 3H), then following the mass action law [37], one is tempted to conclude that the percentage of V$_B$ that combine with Mo$_{\text{ad}}$ is $\exp[(E_{\text{binding}} - E_{\text{Mo}})/k_BT]$. Thus Mo$_{\text{ad}} + V_B$ pairing will approach completion as E_{binding} overpowers E_{Mo}. However, this requirement on E_{binding} can be alleviated. Just like defects can be immobilized by high migration barriers and become out of equilibrium [37], so can *defect pairs be locked by high binding energies and become out of equilibrium*. Removing each H and Mo from V$_B$ requires 2.3–2.7 eV and 9.1 eV, respectively, so if unbinding occurs at 1000 K, our MoS$_2$ growth temperature, it would occur at rates of $2-200$ s^{-1} and 10^{-32} s^{-1}. Therefore, as along as $E_{\text{binding}} > 0$, Mo$_{\text{ad}}$ will irreversibly replace H due to the much longer timescale of its unbinding. Indeed, $E_{\text{binding}} = 9.1-7.7 = 1.4$ eV for Mo$_{\text{ad}}$.

The earliest event in the formation of V$_B$ + Mo$_{\text{ad}}$ is presumably the binding of a Mo atom to a V$_B$ (V$_B$ are common in hBN [38]) by 9.6 eV, consistent with the reported strong binding between V$_B$ and transition metal atoms in general [39] and the strong binding of transition metal atoms to pyridinic-nitrogen defects in graphene in particular [40] (structurally similar to V$_B$). The under-coordinated Mo atoms available in partially decomposed MOCVD precursors such as Mo(CO)$_x$ or CVD precursors such as MoO$_x$ or MoS$_x$O$_y$ should also bind strongly to V$_B$ (see Ref. [41] for the case of MoO$_3$). The full growth kinetics for the nucleation of MoS$_2$ at a V$_B$ is beyond the scope of the present study, but the most plausible such route begins with the V$_B$-bound Mo adatom first coordinating to ambient S. Strikingly, these sulfur atoms can then form the V$_B$ + Mo$_{\text{ad}}$ interlayer Frenkel pair by incorporating

FIG. 2. A Mo interstitial atom (red) between MoS$_2$ and a V$_B$ in hBN in a $4 \times 4/(5 \times 5)$ supercell equilibrates to a 5.05 Å interlayer spacing, which is very close to the 4.96 Å spacing of pristine MoS$_2$ on pristine hBN. The individual separations of Mo from each of these sheets in isolation also sum to essentially the same value. Thus Mo + V$_B$ on hBN can nucleate the growth of a MoS$_2$ overlayer with surprisingly little deformation of the ideal bilayer spacing.

directly into a MoS$_2$ overlayer that sits above the hBN layer. Figure 2 shows this configuration with a structurally relaxed 4×4 MoS$_2$ on 5×5 hBN supercell: the 5.05 Å interlayer separation is very close to the 4.96 Å vdW separation of *pristine* MoS$_2$ on hBN. Thus the Mo interstitial above V$_B$ essentially "takes up no space" in the interlayer gallery. In a further interesting coincidence, the adatom heights of two "constituent" systems, Mo above V$_B$ + hBN (2.15 Å) and Mo above pristine MoS$_2$ (2.90 Å), sum to nearly the same value.

The energetic comparisons between the 0/180° stacking described earlier are now reexamined, including a V$_B$ + Mo$_{\text{ad}}$ complex, with very different results. The orientation where the three sulfur atoms and three nitrogen atoms nearest to the Mo interstitial are staggered is strongly favored, by 0.88 eV per Mo interstitial, over the opposite orientation where they are eclipsed (Fig. 3). A similar preference is well-known in the conformational isomers of molecules such as ethane [42].
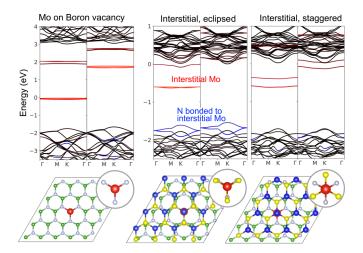

FIG. 3. Spin-polarized DFT band structures of a Mo atom bound to a V$_B$, and a Mo$_{\text{ad}}$ + V$_B$ complex with an eclipsed and staggered configuration; Fermi levels are set to zero. The two band structures in each panel represent the majority and minority spin channel. States localized on the interstitial Mo and its three nearest-neighbor N atoms are colored red and blue, respectively. Nitrogen levels in the valence band rise in energy when eclipsed, reflecting the repulsion between the N and S atoms bonded to the interstitial Mo.
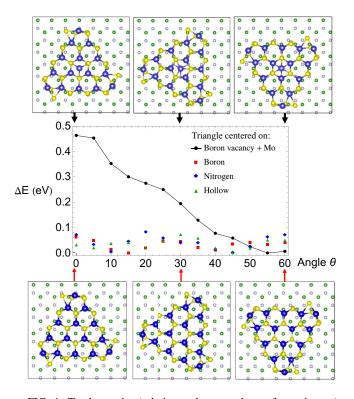
FIG. 4. Total energies (relative to the ground state for each case) of finite MoS_2 flakes on monolayer hBN with a boron vacancy and Mo interstitial (black, connected plot). The weaker stacking energy variations without $V_B + Mo_{ad}$ are shown in the scattered plots in color, where the center of the flake lies above a B (red squares), N (blue diamonds), or hollow site (green triangles) during rotation.

This defect-mediated orientational preference appears to be generic, as we also found substantial (~0.5 eV) orientational preferences for $V_N + Mo_{ad}$ and other defect-pair structures (see Fig. S3). Finally, to demonstrate the absence of local minima at other intermediate orientations and the robustness of this orientation preference against edge effects, we examined *finite* MoS_2 triangles on hBN with interstitial $V_B + Mo_{ad}$ at the centers and again found a substantial preference of ~0.5 eV, as shown by the connected black dots in Fig. 4 (details are discussed in the Supplemental Material [41]). The much weaker variation in the stacking energy of the same flake on hBN without $V_B + Mo_{ad}$ is shown in the scattered plots, where the center of the flake lies above a B (red squares), N (blue diamonds), or hollow site (green triangles) as the flake is rotated.

Electronic structure calculations reveal the origin of the strong binding of $V_B + Mo_{ad}$ and its mechanism of orientation control: the interlayer Frenkel pair is also a donor-acceptor pair. A V_B accepts three electrons from a transition metal (e.g., Mo) upon adsorption [39], leaving three degenerate occupied Mo d orbitals within the band gap, as shown by the occupied red bands in Fig. 3 (the two columns in each panel are for the majority and minority spin channel). When a MoS_2 layer is added, these midgap states split differently for the two stacking orientations, but with similar summed band energies. In contrast, the eigenvalues for the orbitals of the nitrogen atoms bonded to the Mo interstitial lie much higher
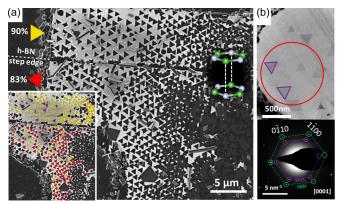

FIG. 5. (a) SEM image of triangular MoS_2 flakes on hBN. An hBN step edge separates two regions, each with 83% or 90% of the flakes at the same orientation. Inset shows the same image color-coded by orientation. (b) TEM image of triangular MoS_2 flakes grown on freestanding hBN where its crystallinity and alignment with the hBN substrate are verified by the selected area electron diffraction from the circled area.

for the eclipsed geometry, due to the repulsion (with possible electrostatic and steric contributions [42,43]) from the sulfur above (blue bands in Fig. 3). This effect has been verified with hybrid functional calculations (Fig. S4), which generally provide more accurate defect level positions and formation energies [34,35]. This mechanism of orientation preference does not extend to bilayer MoS_2 with a Mo interstitial, which does not charge transfer to either sheet.

IV. GROWTH EXPERIMENTS ON PRISTINE AND PLASMA-TREATED HEXAGONAL BN

Taken in total, these results demonstrate how $V_B + Mo_{ad}$ and similar defects could induce epitaxial growth of MoS_2 with full orientation control. Is this mechanism borne out by experiment? To this end, MoS_2 was grown on freestanding hBN (on a TEM grid) as well as on Si/SiO_2-supported hBN using a PVT growth protocol that prioritizes the initial heterogeneous nucleation of metal species at the boron vacancy sites (see Ref. [41] and Fig. S5 for details). Raman and photoluminescence spectroscopy of this MoS_2 grown on hBN are similar to those of free-standing MoS_2, verifying the quality of the hBN substrate (Fig. S6, in contrast to MoS_2 on Si/SiO_2). Within the triangular MoS_2 flakes revealed by scanning electron microscopy in Fig. 5(a) (with more images in Fig. S8), ~90% have a single, consistent orientation in the upper region of the hBN substrate. The 0°/180° stacking degeneracy *is nearly fully lifted*. Such flakes can merge into a monolayer film nearly free of inversion domain boundaries, as suggested by annular dark field–scanning transmission electron microscopy (ADF-STEM) images in Fig. S9. A correlation between triangle orientation and the hBN surface polarity is also the most parsimonious explanation for the observed *reversal* of triangle orientation across a step edge in the hBN substrate [dashed line in Fig. 5(a)], noting that the layer polarity of AA′-stacked hBN reverses across an odd-layer number step edge. Although a direct measurement of step height is not available due to its coverage by multilayer MoS_2 and

measurement uncertainty in estimating bulk hBN thicknesses, any other explanation for this reversal would require that an alternative property not related to lattice polarity both change across the step edge and also control the lattice polarity of the MoS₂ flakes. The possibility that the observed orientation inversion reflects an inversion of the thermodynamic or kinetic Wulff shape is also unlikely since step edges do not interrupt Wulff shapes (except for possibly truncating corners), and also since it would imply abrupt spatial changes in the growth conditions, which vary continuously on millimeter length scales. In contrast to the clear orientation preference on hBN, second-layer MoS₂ flakes stacked on the first-layer MoS₂ film [lower right of Fig. 5(a)] lack preferred alignment. The bright-field TEM image and corresponding selected-area electron diffraction [SAED, Fig. 5(b)] confirm a precise alignment of parallel zigzag edges between hBN and MoS₂ (see Fig. S10 for additional characterization). Unlike in Fig. 5(a), both 0/180° orientations are seen in Fig. 5(b) because growth occurred on *both sides* of free-standing hBN.

Direct imaging of single isolated boron vacancies in *multi-layer* hBN substrates that are covered by MoS₂ is not feasible because each imaged hBN lattice site is actually a full atomic column due to the bulk hBN AA′ stacking (see Ref. [38] for a demonstration of the drastic decrease in vacancy visibility when the layer number increases from one to four). While interstitial metal atoms may be more reliably imaged (as reported elsewhere for the WSe₂/hBN system [44]), the defect-mediated orientational control mechanism described here can be tested to a certain degree by establishing that only isolated point defects support full orientation control of MoS₂, i.e., more geometrically complex defects in hBN such as multivacancy voids or step edges should *not* facilitate orientational epitaxy. To test this hypothesis, a population of vacancies was introduced through a pregrowth reactive ion etching of suspended hBN films for 0, 10, or 30 sec [41]. MoS₂ flakes were then grown on these plasma-treated hBN substrates with identical precursors, growth temperatures, and growth times. ADF-STEM imaging [Figs. 6(a)–6(c)] along with SAED [Figs. 6(d)–6(f)] reveal that plasma treatment increases the total number of MoS₂ flakes (likely due to a higher density of nucleation sites) while losing epitaxy, as quantified by the histograms of MoS₂ misorientation angles with respect to hBN in Figs. 6(g)–6(i) (see also Fig. S11). High-resolution electron microscopy images [Figs. 6(j)–6(l)] confirm that ion-irradiated hBN contains a much higher defect population with higher complexity, including many larger-scale voids and associated step edges, consistent with the loss of the stagger/eclipse mechanism around these more geometrically complex defects. Fresh hBN step edges created by etching should significantly promote the growth of MoS₂ flakes with random orientations, as suggested by the observed random orientations of MoS₂ flakes grown at pre-existing step edges (from the hBN sample without plasma treatment, Fig. S12).

V. CONCLUSION

The present work demonstrates that, although vacancies in a crystal are an obvious degradation of *translational* order, their spatially "sharp" physical nature and well-controlled angular structure can paradoxically enhance the sensitivity of
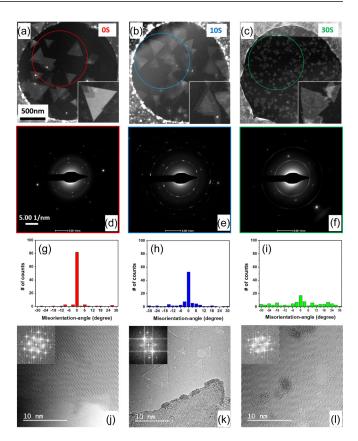

FIG. 6. Effect of different reactive ion etching time. (a)–(c) ADF-STEM images of as-grown MoS₂/hBN heterostructures after 0, 10 or 30 sec of etching, whose degree of epitaxy is examined by (d)–(f) selected area diffraction, yielding (g)–(i) histograms of MoS₂ misorientation angles with respect to hBN. Corresponding (j)–(l) high-resolution (HR)TEM images of hBN substrates for different etching times show more complex defect structures in the etched films.

a system to *orientational* order, especially during the critical stage of nucleation, by accentuating orientation-dependent interlayer interactions. Defect-assisted orientational epitaxy exploits the identical structure and orientation of a given type of point defect (e.g., V_B) across a polar crystalline substrate. Even given full orientation uniformity and coalescence, *translational* mismatch is still a concern upon the merging of two grains. However, no such boundaries have been reported for TMDs thus far, presumably due to being outcompeted energetically by perfect stitches (see Fig. S9 and Ref. [45]). If there are no strong substrate registry effects (e.g., TMDs on hBN), the strain energy distributed deep into the flake interior across a lateral distance D from the boundary scales as $D(1/D)^2 = 1/D$, so stitching is more favorable than grain boundary formation for large D (i.e., large-enough flakes). To our knowledge, the only report of zero-tilt boundaries in a 2D material so far is for graphene on high-registry Ni [46]. Even misoriented grains almost always stitch together tightly into dense mirror boundaries (a chain of rhombi [9,45]), underlining the propensity for film coalescence in these systems. One can thus envision defect-enhanced epitaxy (also possibly seed molecules [17]) as providing a general means to promote well-oriented layer-by-layer growth of 2D heterostructures.

These insights into the atomistic mechanisms of orientation control can help guide further improvements to film crystallinity, as has been recently achieved in the growth of WSe$_2$ on hBN using metal-organic chemical vapor deposition (MOCVD) with a strong suppression of inversion domains [44]. For example, introducing transition metal precursors of the same kind as the parent film can minimize the trapping of competing precursors that may otherwise "poison" substrate vacancies. Coalescence techniques [47] can then be combined with orientational control to achieve monocrystallinity.

APPENDIX A: ORIENTATION PREFERENCE OF PRISTINE PERIODIC STRUCTURES

In 5×5 hBN $+ 4 \times 4$ MoS$_2$ supercells, the relative energies of different stacking orientations and translations are calculated with three implementations of vdW corrections and are shown in Fig. 7. The three implementations agree that energies are not sensitive to translation (as shown by the clustering of the dots at $0°$ and $60°$, respectively), while the orientation preference increases from 0.1 meV (per MoS$_2$) for vdW-DF2 to 0.3 meV for DFT-D3, and to 0.5 meV for DFT-TS. Alternatively, a $\sqrt{21} \times \sqrt{21}$ h-BN supercell ($5\mathbf{a} + 1\mathbf{b}$)

and a $\sqrt{13} \times \sqrt{13}$ MoS$_2$ supercell ($4\mathbf{A} + 1\mathbf{B}$) can be used to construct a heterostructure with strain less than 1% [48], where $\mathbf{a}$ and $\mathbf{b}$ are the lattice vectors for h-BN and $\mathbf{A}$ and $\mathbf{B}$ are for MoS$_2$. Since both supercell lattice vectors ($5\mathbf{a} + 1\mathbf{b}$) and ($4\mathbf{A} + 1\mathbf{B}$) lie about $15°$ degrees away from the zigzag direction, the same heterostructure supercell can fit stacking geometries close to $0°$, $30°$, and $60°$ (more accurately, $3°$, $25°$, $35°$, and $57°$). Thus the two near-ground-state stackings ($3°$ and $57°$) can be fairly compared with the two intermedite twist angles ($25°$ and $35°$), i.e., with the remaining 1% artifical strain cancelled out when comparing relative energies. The energy difference between $3°$ and $57°$ is 0.4 meV per MoS$_2$ unit, consistent with the estimate using the $5 \times 5 + 4 \times 4$ heterostructure supercell, while near-$30°$ stackings are about 2 meV per MoS$_2$ unit above the $0°$ ground state. This barrier should span over a wide range between $0°$ and $60°$ [49], implying that, if edge effects are ignored, a flake would translate and rotate on the substrate with negligible corrugation until it is trapped by a $0°$ or $60°$ stacking.

APPENDIX B: VACANCY TYPES IN HEXAGONAL BN

To determine whether intrinsic hBN defects with complexities higher than monovacancies need to be considered, we calculated defect formation energies of V$_B$, V$_N$, divacancy V$_{BN}$, their various hydrogen passivated complexes, and sulfur substitution of nitrogen S$_N$, as functions of the nitrogen chemical potential μ_N and the Fermi level (for charged defects) within density functional theory. Calculation methods closely follow prior studies with similar results [36,50–52], where potential alignment for the correction of spurious electrostatic interactions in supercell calculations is performed following the Freysoldt-Neugebauer-Van de Walle scheme [53] as implemented in Ref. [54]; parameters for the model dielectric profile of hBN follow those of Ref. [55] where the in-plane and out-of-plane dielectric constant of the hBN slab is properly defined. The correction energies for various supercell sizes and charged states are shown in Fig. 8(a) where each
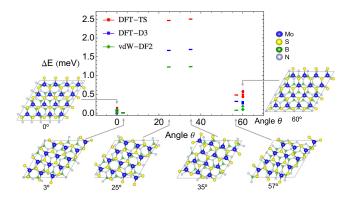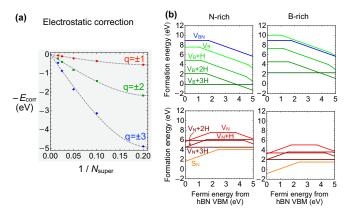

FIG. 7. Relative energies (per MoS$_2$ unit) of different stacking orientations and translations calculated with three implementations of vdW corrections. Point markers are computed with $5 \times 5 + 4 \times 4$ supercells and bar markers are computed with $\sqrt{21} \times \sqrt{21} + \sqrt{13} \times \sqrt{13}$ supercells. The energy difference between the two stable stacking orientations of $0°$ and $60°$ is small compared with the barrier separating them (at intermediate twist angles).

FIG. 8. (a) Corrections to spurious electrostatic interactions in supercell geometries of $N_{super} \times N_{super} \times 1$, for charged states of $q = \pm 1$, ± 2, and ± 3. (b) Formation energies of V$_B$, V$_N$, and V$_{BN}$, as a function of the Fermi level at two nitrogen chemical potentials. Both V$_B$ and V$_N$ are stabilized by H passivation and are favored against V$_{BN}$ over a wide Fermi energy range.

extrapolation towards $N_{super} \to \infty$ (using the functional form of Ref. [54]) is set to zero. The final correction energies for the $N_{super} \times N_{super} \times 1 = 5 \times 5 \times 1$ supercell geometry we used are $+0.55$, $+2.18$, and $+4.90$ eV for $q = \pm 1$, ± 2, and ± 3. The experimentally accessible μ_N is limited within $\mu_N = E(N_2)$ and $\mu_N = E(hBN) - E(\alpha\text{-Boron})$, corresponding to N-rich and B-rich conditions. The chemical potentials for hydrogen and sulfur are set to $E(H_2)$ and $E(\alpha\text{-Sulfur})$. As shown in Fig. 8(b), both hydrogen passivated V_B and V_N are favored against V_{BN} over a wide Fermi energy range under N-rich and B-rich conditions. For unpassivated V_B and V_N, at least one is favored against V_{BN} over the same range. Thus the hBN substrate likely hosts a predominate population of the most favorable *monovacancy* point defect, each serving as a nucleation site for MoS$_2$, with consistent orientations. These results also reflect a strong binding between sulfur and V_N into S_N (similar to the highly stable O_N impurity in Ref. [36]), since its $+1$ charged state is isoelectronic to pristine hBN. The strong S-V_N binding and Mo-V_B binding (see discussion in main text) are consistent with the STEM image in Ref. [44] revealing transition metal and chalcogen atoms always trapped at different sublattices of hBN.

[1] H. Zeng, J. Dai, W. Yao, D. Xiao, and X. Cui, Nat. Nanotechnol. **7**, 490 (2012).

[2] K. F. Mak, K. He, J. Shan, and T. F. Heinz, Nat. Nanotechnol. **7**, 494 (2012).

[3] W. Wu, L. Wang, Y. Li, F. Zhang, L. Lin, S. Niu, D. Chenet, X. Zhang, Y. Hao, T. F. Heinz, J. Hone, and Z. L. Wang, Nature (London) **514**, 470 (2014).

[4] H. Zhu, Y. Wang, J. Xiao, M. Liu, S. Xiong, Z. J. Wong, Z. Ye, Y. Ye, X. Yin, and X. Zhang, Nat. Nanotechnol. **10**, 151 (2014).

[5] M. Okada, T. Sawazaki, K. Watanabe, T. Taniguch, H. Hibino, H. Shinohara, and R. Kitaura, ACS Nano **8**, 8273 (2014).

[6] A. Yan, J. Velasco, S. Kahn, K. Watanabe, T. Taniguchi, F. Wang, M. F. Crommie, and A. Zettl, Nano Lett. **15**, 6324 (2015).

[7] W. Auwärter, M. Muntwiler, J. Osterwalder, and T. Greber, Surf. Sci. **545**, L735 (2003).

[8] F. Orlando, P. Lacovig, L. Omiciuolo, N. G. Apostol, R. Larciprete, A. Baraldi, and S. Lizzit, ACS Nano **8**, 12063 (2014).

[9] W. Zhou, X. Zou, S. Najmaei, Z. Liu, Y. Shi, J. Kong, J. Lou, P. M. Ajayan, B. I. Yakobson, and J.-C. Idrobo, Nano Lett. **13**, 2615 (2013).

[10] K. Kang, S. Xie, L. Huang, Y. Han, P. Y. Huang, K. F. Mak, C.-J. Kim, D. Muller, and J. Park, Nature (London) **520**, 656 (2015).

[11] N. V. Tarakina, S. Schreyeck, M. Luysberg, S. Grauer, C. Schumacher, G. Karczewski, K. Brunner, C. Gould, H. Buhmann, R. E. Dunin-Borkowski, and L. W. Molenkamp, Adv. Mater. Interfaces **1**, 1400134 (2014).

[12] D. G. Schlom and J. S. Harris, in *Molecular Beam Epitaxy* (Elsevier, Amsterdam, 1995), pp. 505–622.

[13] K. I. Bolotin, F. Ghahari, M. D. Shulman, H. L. Stormer, and P. Kim, Nature (London) **462**, 196 (2009).

[14] C. R. Dean, A. F. Young, P. Cadden-Zimansky, L. Wang, H. Ren, K. Watanabe, T. Taniguchi, P. Kim, J. Hone, and K. L. Shepard, Nat. Phys. **7**, 693 (2011).

[15] X. Du, I. Skachko, F. Duerr, A. Luican, and E. Y. Andrei, Nature (London) **462**, 192 (2009).

[16] Y. Zhang, Y.-W. Tan, H. L. Stormer, and P. Kim, Nature (London) **438**, 201 (2005).

[17] X. Ling, Y.-H. Lee, Y. Lin, W. Fang, L. Yu, M. S. Dresselhaus, and J. Kong, Nano Lett. **14**, 464 (2014).

[18] S. Wang, X. Wang, and J. H. Warner, ACS Nano **9**, 5246 (2015).

[19] L. Fu, Y. Sun, N. Wu, R. G. Mendes, L. Chen, Z. Xu, T. Zhang, M. H. Rümmeli, B. Rellinghaus, D. Pohl, L. Zhuang, and L. Fu, ACS Nano **10**, 2063 (2016).

[20] Y. Shi, W. Zhou, A.-Y. Lu, W. Fang, Y.-H. Lee, A. L. Hsu, S. M. Kim, K. K. Kim, H. Y. Yang, L.-J. Li, J.-C. Idrobo, and J. Kong, Nano Lett. **12**, 2784 (2012).

[21] T. Georgiou, R. Jalil, B. D. Belle, L. Britnell, R. V. Gorbachev, S. V. Morozov, Y.-J. Kim, A. Gholinia, S. J. Haigh, O. Makarovsky, L. Eaves, L. A. Ponomarenko, A. K. Geim, K. S. Novoselov, and A. Mishchenko, Nat. Nanotechnol. **8**, 100 (2012).

[22] B. Hunt, J. D. Sanchez-Yamagishi, A. F. Young, M. Yankowitz, B. J. LeRoy, K. Watanabe, T. Taniguchi, P. Moon, M. Koshino, P. Jarillo-Herrero, and R. C. Ashoori, Science **340**, 1427 (2013).

[23] C.-H. Lee, G.-H. Lee, A. M. van der Zande, W. Chen, Y. Li, M. Han, X. Cui, G. Arefe, C. Nuckolls, T. F. Heinz, J. Guo, J. Hone, and P. Kim, Nat. Nanotechnol. **9**, 676 (2014).

[24] S. Larentis, J. R. Tolsma, B. Fallahazad, D. C. Dillen, K. Kim, A. H. MacDonald, and E. Tutuc, Nano Lett. **14**, 2039 (2014).

[25] O. Lopez-Sanchez, E. Alarcon Llado, V. Koman, A. Fontcuberta i Morral, A. Radenovic, and A. Kis, ACS Nano **8**, 3042 (2014).

[26] X. Cui, G.-H. Lee, Y. D. Kim, G. Arefe, P. Y. Huang, C.-H. Lee, D. A. Chenet, X. Zhang, L. Wang, F. Ye, F. Pizzocchero, B. S. Jessen, K. Watanabe, T. Taniguchi, D. A. Muller, T. Low, P. Kim, and J. Hone, Nat. Nanotechnol. **10**, 534 (2015).

[27] C. R. R. Dean, A. F. F. Young, I. Meric, C. Lee, L. Wang, S. Sorgenfrei, K. Watanabe, T. Taniguchi, P. Kim, K. L. L. Shepard, and J. Hone, Nat. Nanotechnol. **5**, 722 (2010).

[28] J. He, K. Hummer, and C. Franchini, Phys. Rev. B **89**, 075409 (2014).

[29] G. Constantinescu, A. Kuc, and T. Heine, Phys. Rev. Lett. **111**, 036104 (2013).

[30] S. Grimme, J. Antony, S. Ehrlich, and H. Krieg, J. Chem. Phys. **132**, 154104 (2010).

[31] A. Tkatchenko and M. Scheffler, Phys. Rev. Lett. **102**, 073005 (2009).

[32] K. Lee, É. D. Murray, L. Kong, B. I. Lundqvist, and D. C. Langreth, Phys. Rev. B **82**, 081101 (2010).

[33] D. Fu, X. Zhao, Y. Zhang, L. Li, H. Xu, A. Jang, S. I. Yoon, P. Song, S. M. Poh, T. Ren, Z. Ding, W. Fu, T. J. Shin, H. S. Shin, S. T. Pantelides, W. Zhou, and K. P. Loh, J. Am. Chem. Soc. **139**, 9392 (2017).

[34] H.-P. Komsa and A. V. Krasheninnikov, Phys. Rev. B **91**, 125304 (2015).

[35] C. Freysoldt, B. Grabowski, T. Hickel, J. Neugebauer, G. Kresse, A. Janotti, and C. G. Van de Walle, Rev. Mod. Phys. **86**, 253 (2014).

[36] L. Weston, D. Wickramaratne, M. Mackoit, A. Alkauskas, and C. G. Van de Walle, Phys. Rev. B **97**, 214104 (2018).

[37] C. G. Van de Walle and J. Neugebauer, J. Appl. Phys. **95**, 3851 (2004).

[38] N. Alem, R. Erni, C. Kisielowski, M. D. Rossell, W. Gannett, and A. Zettl, Phys. Rev. B **80**, 155425 (2009).

[39] B. Huang, H. Xiang, J. Yu, and S. H. Wei, Phys. Rev. Lett. **108**, 206802 (2012).

[40] Y.-C. Lin, P.-Y. Teng, C.-H. Yeh, M. Koshino, P.-W. Chiu, and K. Suenaga, Nano Lett. **15**, 7408 (2015).

[41] See Supplemental Material at http://link.aps.org/supplemental/10.1103/PhysRevB.99.155430 for additional details on first-principles calculations [56–65], orientation preference for finite structures [66], alternative defect pairs, hybrid functional calculations [67], growth protocols [68–71], characterization by Raman spectroscopy, photoluminescence, energy-dispersive spectroscopy, and electron energy-loss spectroscopy [72–75], reactive ion etching, quantification of the degree of epitaxy upon etching [76], and an analysis on possible residual strain in the hBN substrate [77–81].

[42] Y. Mo, Wiley Interdiscip. Rev. Comput. Mol. Sci. **1**, 164 (2011).

[43] S. Liu, J. Chem. Phys. **126**, 244103 (2007).

[44] X. Zhang, F. Zhang, Y. Wang, D. S. Schulman, T. Zhang, A. Bansal, N. Alem, S. Das, V. H. Crespi, M. Terrones, and J. M. Redwing, ACS Nano **13**, 3341 (2019).

[45] H. Yu, Z. Yang, L. Du, J. Zhang, J. Shi, W. Chen, P. Chen, M. Liao, J. Zhao, J. Meng, G. Wang, J. Zhu, R. Yang, D. Shi, L. Gu, and G. Zhang, Small **13**, 1603005 (2017).

[46] J. Lahiri, Y. Lin, P. Bozkurt, I. I. Oleynik, and M. Batzill, Nat. Nanotechnol. **5**, 326 (2010).

[47] X. Zhang, T. H. Choudhury, M. Chubarov, Y. Xiang, B. Jariwala, F. Zhang, N. Alem, G.-C. Wang, J. A. Robinson, and J. M. Redwing, Nano Lett. **18**, 1049 (2018).

[48] H. P. Komsa and A. V. Krasheninnikov, Phys. Rev. B **88**, 085318 (2013).

[49] D. Dumcenco, D. Ovchinnikov, K. Marinov, P. Lazić, M. Gibertini, N. Marzari, O. L. Sanchez, Y.-C. Kung, D. Krasnozhon, M.-W. Chen, S. Bertolazzi, P. Gillet, A. Fontcuberta i Morral, A. Radenovic, and A. Kis, ACS Nano **9**, 4611 (2015).

[50] S. Okada, Phys. Rev. B **80**, 161404 (2009).

[51] W. Orellana and H. Chacham, Phys. Rev. B **63**, 125205 (2001).

[52] B. Huang and H. Lee, Phys. Rev. B **86**, 245406 (2012).

[53] C. Freysoldt, J. Neugebauer, and C. G. Van de Walle, Phys. Rev. Lett. **102**, 016402 (2009).

[54] M. H. Naik and M. Jain, Comput. Phys. Commun. **226**, 114 (2018).

[55] H. P. Komsa, N. Berseneva, A. V. Krasheninnikov, and R. M. Nieminen, Phys. Rev. X **4**, 031044 (2014).

[56] J. P. Perdew, K. Burke, and M. Ernzerhof, Phys. Rev. Lett. **77**, 3865 (1996).

[57] J. P. Perdew, K. Burke, and M. Ernzerhof, Phys. Rev. Lett. **78**, 1396 (1997).

[58] G. Kresse and D. Joubert, Phys. Rev. B **59**, 1758 (1999).

[59] P. E. Blöchl, Phys. Rev. B **50**, 17953 (1994).

[60] G. Kresse and J. Furthmüller, Phys. Rev. B **54**, 11169 (1996).

[61] T. Björkman, A. Gulans, A. V. Krasheninnikov, and R. M. Nieminen, J. Phys. Condens. Matter **24**, 424218 (2012).

[62] T. Björkman, A. Gulans, A. V. Krasheninnikov, and R. M. Nieminen, Phys. Rev. Lett. **108**, 235502 (2012).

[63] T. Bučko, S. Lebègue, J. Hafner, and J. G. Ángyán, Phys. Rev. B **87**, 064110 (2013).

[64] J. Heyd, G. E. Scuseria, and M. Ernzerhof, J. Chem. Phys. **118**, 8207 (2003).

[65] J. Heyd, G. E. Scuseria, and M. Ernzerhof, J. Chem. Phys. **124**, 219906 (2006).

[66] J. Kibsgaard, T. F. Jaramillo, and F. Besenbacher, Nat. Chem. **6**, 248 (2014).

[67] C. Attaccalite, M. Bockstedte, A. Marini, A. Rubio, and L. Wirtz, Phys. Rev. B **83**, 144115 (2011).

[68] F. Zhang, C. Erb, L. Runkle, X. Zhang, and N. Alem, Nanotechnology **29**, 025602 (2018).

[69] F. Zhang, M. A. AlSaud, M. Hainey, K. Wang, J. M. Redwing, and N. Alem, Microsc. Microanal. **22**, 1640 (2016).

[70] F. Zhang, K. Momeni, M. A. AlSaud, A. Azizi, M. F. Hainey, J. M. Redwing, L. Q. Chen, and N. Alem, 2D Mater. **4**, 025029 (2017).

[71] M. Bosi, RSC Adv. **5**, 75500 (2015).

[72] C. Lee, H. Yan, L. E. Brus, T. F. Heinz, J. Hone, and S. Ryu, ACS Nano **4**, 2695 (2010).

[73] A. Splendiani, L. Sun, Y. Zhang, T. Li, J. Kim, C. Y. Chim, G. Galli, and F. Wang, Nano Lett. **10**, 1271 (2010).

[74] K. F. Mak, C. Lee, J. Hone, J. Shan, and T. F. Heinz, Phys. Rev. Lett. **105**, 136805 (2010).

[75] N. Alem, Q. M. Ramasse, C. R. Seabourne, O. V. Yazyev, K. Erickson, M. C. Sarahan, C. Kisielowski, A. J. Scott, S. G. Louie, and A. Zettl, Phys. Rev. Lett. **109**, 205502 (2012).

[76] J. C. Meyer, A. Chuvilin, G. Algara-Siller, J. Biskupek, and U. Kaiser, Nano Lett. **9**, 2683 (2009).

[77] M. Neek-Amal, J. Beheshtian, A. Sadeghi, K. H. Michel, and F. M. Peeters, J. Phys. Chem. C **117**, 13261 (2013).

[78] W. Yang, G. Chen, Z. Shi, C.-C. Liu, L. Zhang, G. Xie, M. Cheng, D. Wang, R. Yang, D. Shi, K. Watanabe, T. Taniguchi, Y. Yao, Y. Zhang, and G. Zhang, Nat. Mater. **12**, 792 (2013).

[79] A. Summerfield, A. Davies, T. S. Cheng, V. V. Korolkov, Y. Cho, C. J. Mellor, C. T. Foxon, A. N. Khlobystov, K. Watanabe, T. Taniguchi, L. Eaves, S. V. Novikov, and P. H. Beton, Sci. Rep. **6**, 22440 (2016).

[80] J. Wu, B. Wang, Y. Wei, R. Yang, and M. Dresselhaus, Mater. Res. Lett. **1**, 200 (2013).

[81] J. A. Oliveira, W. B. De Almeida, and H. A. Duarte, Chem. Phys. Lett. **372**, 650 (2003).